Supporting Information:

for

<u>A Chiral Heliconical Ground State of Nanoscale Pitch</u>
<u>in a Nematic Liquid Crystal of Achiral Molecular Dimers</u>

Dong Chen[1], Jan H. Porada[2],
Justin B. Hooper[3], Arthur Klittnick[1], Yongqiang Shen[1], Michael R. Tuchband[1]
Eva Korblova[2], Dmitry Bedrov[3], David M. Walba[2],
Matthew A. Glaser[1], Joseph E. Maclennan[1] and Noel A. Clark[1]

[1] Department of Physics and Liquid Crystal Materials Research Center,
University of Colorado, Boulder, CO 80309-0390

[2] Department of Chemistry and Biochemistry and Liquid Crystal Materials Research Center,
University of Colorado, Boulder, CO 80309-0215

[3] Department of Materials Science and Engineering, University of Utah, Salt Lake City, UT 84112, and Liquid Crystal Materials Research Center, University of Colorado, Boulder, CO 80309-0215

1. Synthesis of CB7CB
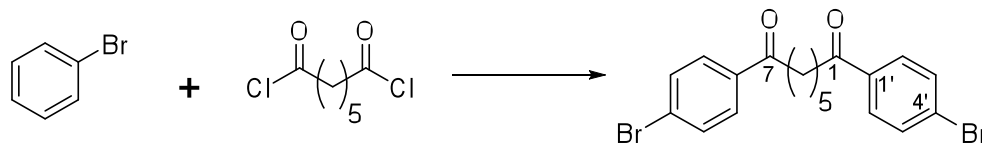
1,7-bis(4'-bromophenyl)heptane-1,7-dione: A solution of 5.00g (25 mmol) pimeloyl chloride in 5 ml (45 mmol) bromobenzene was slowly dropped into an ice-cooled and stirred suspension of 7.07g (53 mmol) aluminum trichloride in 30 ml (285 mmol) bromobenzene under argon. The reaction mixture was stirred for 12 hours and allowed to warm to room temperature, before it was poured on ice water (200 ml). The organic phase was extracted with dichloromethane and washed once with sodium hydrogen carbonate solution, once with water, and then was dried over magnesium sulfate. The solvent and excess bromobenzene was removed in vacuum and the product was recrystallized from ethanol yielding 10.07 g (23 mmol, 92%) of colorless crystals.

^{1}H NMR (300 MHz, CDCl$_3$) δ 7.81 (d, J = 8.8 Hz, 4H; 2'-H and 6'-H), 7.60 (d, J = 8.8 Hz, 4H; 3'-H and 5'-H), 2.95 (t, J = 7.3 Hz, 4H; 2-CH$_2$ and 6-CH$_2$), 1.87 – 1.69 (m, 4H; 3-CH$_2$ and 5-CH$_2$), 1.56 – 1.39 (m, 2H; 4-CH$_2$).

^{13}C NMR (75 MHz, CDCl$_3$) δ 199.26 (s; C-1 and C-7), 135.82 (s; C-1'), 132.04 (d; C-3' and C- 5'), 129.71 (d; C-2' and C- 6'), 128.26 (s; C-4'), 38.37 (t; C-2 and C-6), 28.97 (t; C-4), 24.02 (t; C-3 and C-5).
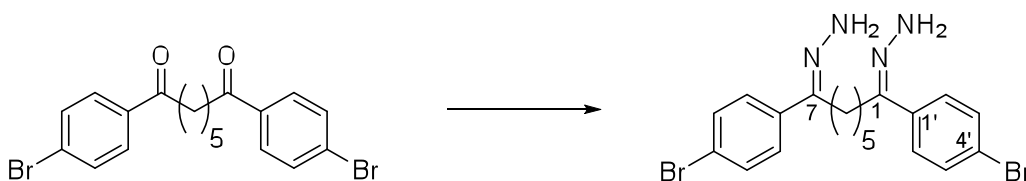
1,7-bis(4'-bromophenyl)-1,7-dihydrazonoheptane: 10.00g (22.8 mmol) 1,7-bis(4-bromophenyl)heptane-1,7-dione were dissolved in 70 ml abs. ethanol and 5.5 ml hydrazine hydrate were added. The solution was refluxed for 12 hours, cooled to room temperature and was further cooled in the freezer. The precipitate was filtered off, giving 6.244 g (13.4 mmol, 59%) of 1,7-bis(4-bromophenyl)-1,7-dihydrazonoheptane as a slightly yellow powder.

^{1}H NMR (300 MHz, CDCl$_3$) δ 7.47 (m, 8H; 2'-H, 3'-H, 5'-H and 6'-H), 5.42 (s, 4H; NH$_2$), 2.70 – 2.38 (m, 4H; 2-CH$_2$ and 6-CH$_2$), 1.73 – 1.31 (m, 6H; 3-CH$_2$, 4-CH$_2$ and 5-CH$_2$).

^{13}C NMR (75 MHz, CDCl$_3$) δ 149.19 (s; C-1 and C-7), 137.51 (s; C-1'), 131.58 (d; C-3' and C- 5'), 127.21 (d; C-2' and C- 6'), 122.27 (s; C-4'), 30.17 (t; C-4), 25.12, 24.92 (t; C-2, C-3, C-5 and C-6).
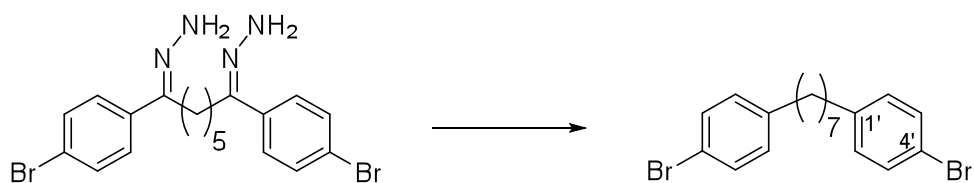
1,7-bis(4'-bromophenyl)heptane: 6.06 g (13.0 mmol) of 1,7-bis(4-bromophenyl)-1,7-dihydrazonoheptane were solved in 100 ml dry toluene and 7.29g (65.0 mmol) of potassium tert.-butoxide were added. The solution was refluxed under argon for 48 hours, cooled to room temperature and poured into 100 ml ice-cooled 1M HCl. The organic layer was separated and the aqueous phase was extracted with dichloromethane. The combined organic phases were washed once with water, once with brine, and then were dried over magnesium sulfate. The solvent was removed and the crude product was recrystallized from ethanol, giving 3.95g (9.6 mmol, 74%) of 1,7-bis(4-bromophenyl)heptane as colorless crystals.

^{1}H NMR (300 MHz, CDCl$_3$) δ 7.39 (d, J = 8.3 Hz, 4H; 3'-H and 5'-H), 7.04 (d, J = 8.4 Hz, 4H; 2'-H and 6'-H), 2.55 (t, J = 7.7 Hz, 4H; 1-CH$_2$ and 7-CH$_2$), 1.65 – 1.50 (m, 4H; 2-CH$_2$ and 6-CH$_2$), 1.42 – 1.22 (m, 6H; 3-CH$_2$, 4-CH$_2$ and 5-CH$_2$).

^{13}C NMR (75 MHz, CDCl$_3$) δ 141.84 (s; C-1 and C-7), 131.38 (d; C-2' and C-6'), 130.29 (d; C-3' and C-5'), 119.40 (s; C-4'), 35.44 (t; C-1 and C-7), 31.38 (t; C-2 and C-6), 29.38 (t; C-4), 29.16 (t; C-3 and C-5).
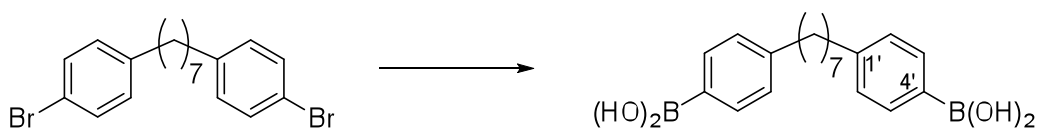
(heptane-1,7-diylbis(4',1'-phenylene))diboronic acid: 3.77g (9.2 mmol) of 1,7-bis(4-bromophenyl)heptane were solved in 50 ml dry THF and cooled to -78°C. 12.5 ml (20 mmol) of n-butyl lithium (1.6M in hexane) were added slowly and the reaction mixture was stirred for 0.5 hours at -78°C. 4.5 ml (40 mmol) trimethyl borate were added and the mixture was allowed to warm to room temperature before 40 ml of 5M HCl were added. The solution was extracted with diethyl ether and the organic phase was washed twice with water, once with brine, and then was dried over magnesium sulfate. The solvent was evaporated and gave 3.07 g (9.0 mmol, 98%) of crude (heptane-1,7-diylbis(4,1-phenylene))diboronic acid as colorless paste, which was used without further purification.
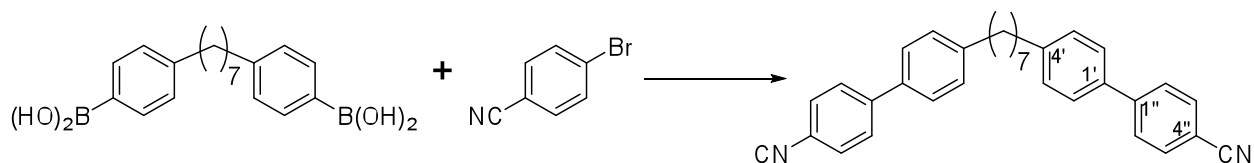
4',4'-(heptane-1,7-diyl)bis(([1',1''-biphenyl]-4''-carbonitrile)): 1.02g (3.0 mmol) (heptane-1,7-diylbis(4,1-phenylene))diboronic acid, 1.20g (6.6 mmol) 4-bromobenzonitrile and 2.07g (15.0 mmol) potassium carbonate were suspended in a mixture of 50 ml ethanol and 10 ml water and degassed by applying vacuum and flushing with argon under ultrasonic irradiation. Then 0.346g (0.3 mmol) tetrakis(triphenylphoshine)palladium(0) were given to the reaction mixture and it was refluxed for 12 hours. The solvent was evaporated in vacuum and 30 ml dichloromethane and 30 ml water were given to the residue. The organic phase was separated, washed twice with water, once with brine, and then was dried over magnesium sulfate. The solvent was evaporated and the crude product was purified chromatographically on silica with dichloromethane as eluent yielding 0.747 g (1.64 mmol, 55%) of 4',4'-(heptane-1,7-diyl)bis(([1',1''-biphenyl]-4''-carbonitrile)) as a colorless solid.

^{1}H NMR (300 MHz, CDCl$_3$) δ 7.75 – 7.62 (m, 8H; 2''-H, 3''-H, 5''-H and 6''-H), 7.51 (d, J = 8.2 Hz, 4H; 2'-H and 6'-H), 7.29 (d, J = 8.5 Hz, 4H; 3'-H and 5'-H), 2.66 (t, J = 7.7 Hz, 4H; 1-CH$_2$ and 7-CH$_2$), 1.75 – 1.56 (m, 4H; 2-CH$_2$ and 6-CH$_2$), 1.46 – 1.32 (m, 6H; 3-CH$_2$, 4-CH$_2$ and 5-CH$_2$).

^{13}C NMR (75 MHz, CDCl$_3$) δ 145.68 (s; C-1''), 143.80 (s; C-4'), 136.58 (s; C-1'), 132.68 (d; C-3'' and C-5''), 129.29 (d; C-3' and C-5'), 127.57 (d; C-2'' and C-6''), 127.19 (d; C-2' and C-6'), 119.15 (s; CN), 110.66 (s; C-4''), 35.72 (t; C-1 and C-7), 31.48 (t; C-2 and C-6), 29.47 (t; C-4), 29.33 (t; C-3 and C-5).

2 – X-Ray Diffraction

X-Ray diffraction was carried out on beamline X10A of the National Synchrotron Light Source (NSLS), Brookhaven National Laboratory. This beamline has a Si 111 double monochromater, typically tuned to around 10 keV. The sample is mounted in an Instec hot stage on a Huber 4-circle goniometer. The point detection arm is equipped with a Ge monochromater to select the direction of diffracted x-rays. The angular resolution, measured by scanning the detector arm through the attenuated direct beam, is typically δq ~ 0.005 nm^{-1} full width at half maximum (FWHM).

3 – Atomistic Computer Simulation

A non-polarizable version of the APPLE&P force field [1] was used in all simulations treating all atoms explicitly. Simulations contained 384 mesogens set up in three-dimensional, periodic orthorhombic simulation cells. All simulations were conducted using the integration scheme proposed by Martyna et al. [2] with time steps of 10^{-2} fs and 0.5×10^{-3} fs for the thermostat and barostat control, respectively. Initially, the mesogens were set up on a regular low-density lattice and then the system was shrunk to the desired dimension, i.e. x and y dimensions about

5.6 nm and 8 nm for the z-direction. During this compression and the subsequent equilibration, the simulations were executed with a biasing potential that aligned the mesogens along the z-axis. The latter was achieved by applying weak forces to cyano groups at the end of each molecule pulling them in opposite directions (+z and -z). As a result, the initially equilibrated configurations were in a well-defined nematic phase (N) with the nematic director aligned along z-direction. Subsequently, the biasing potential was turned off and each system was simulated in the NP_zT ensemble with the z-dimension allowed to fluctuate to achieve the atmospheric pressure in the system, while x and y dimensions were kept fixed. During these simulations the cell dimension in the z-direction fluctuated within ~1.0 Å. The final stress tensor was very close to zero indicating that, as expected for a liquid, no residual stresses remained in the system due to applied constraints on cell dimensions.   Simulations were carried out in the 370 - 410 K temperature range. Production runs were over 20 ns during which no drift in the system energy or order parameters were observed indicating stationary behavior of the targeted equilibrium conditions.

Simulations were conducted with bond lengths constrained using the Shake algorithm [3] to utilize a larger time step. The long-range electrostatic forces were treated by the Ewald summation method. A multiple time step, reversible reference system propagator algorithm [2] was employed with a time step of 0.5 fs for bonding, bending, and torsional forces, a 1.5 fs time step for non-bonded interactions within a 7.0 Å cutoff radius, and a 3.0 fs time step for non-bonded interactions between 7.0 and 11.0 Å and for the reciprocal part of the Ewald summation.

The lowest energy conformation for an alkyl chain is the all-*trans* configuration for the backbone dihedrals which leads to noticeably distinct orientations of the CB half-molecular units, as indicated in Figure 6B and D. In CB7CB the angle, β, between the two CB unit axes is substantially less than β = 180°, forming a banana-like conformation, while CB6CB has an almost linear configuration. However, the energy difference between *trans* (180°) and *gauche* (±60°) dihedral orientations is only 0.5 kcal/mol, which at 370K is less than 1 k_BT of energy and therefore plenty of gauche conformations are expected in a quite flexible alkyl spacer due to thermal fluctuations. Our analysis of dihedral populations shows that in the formed nematic phases, the spacers of both mesogens have on average about 30% of torsions in the *gauche* state and therefore the probability of finding all-*trans* configurations of alkyl spacers is small.
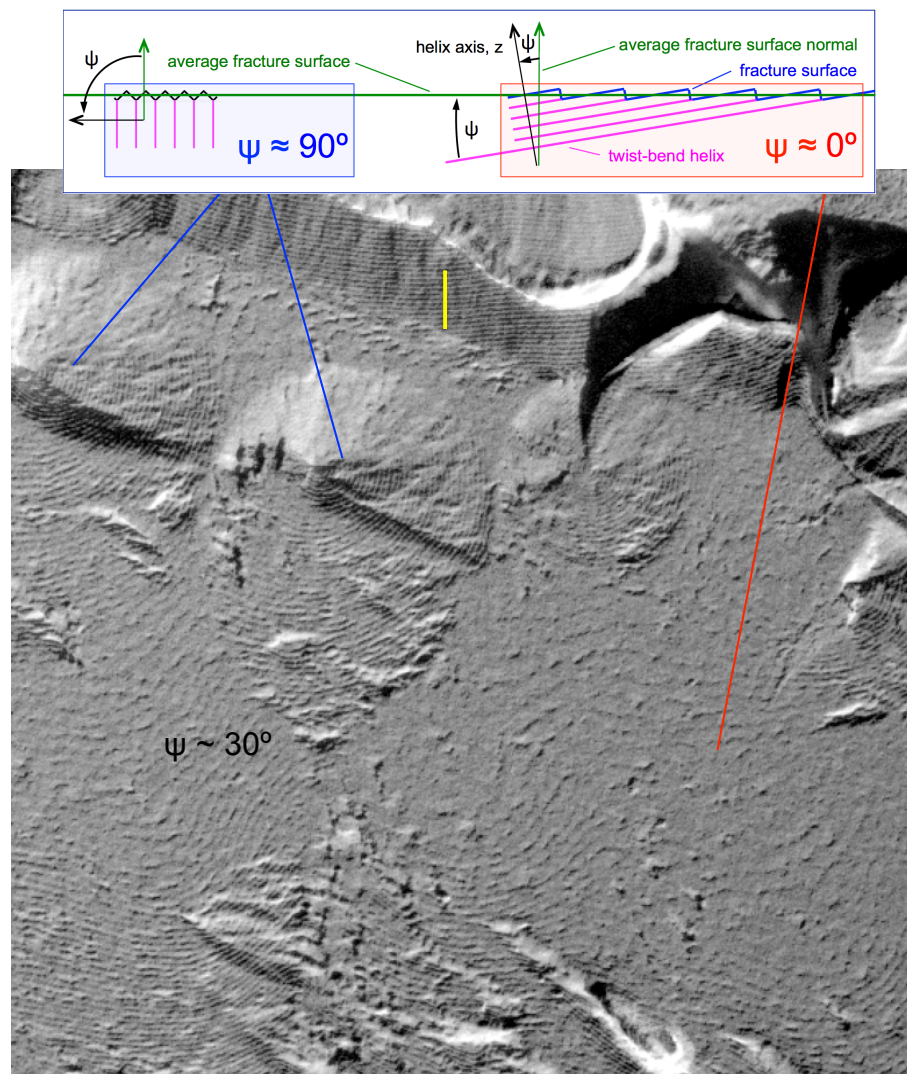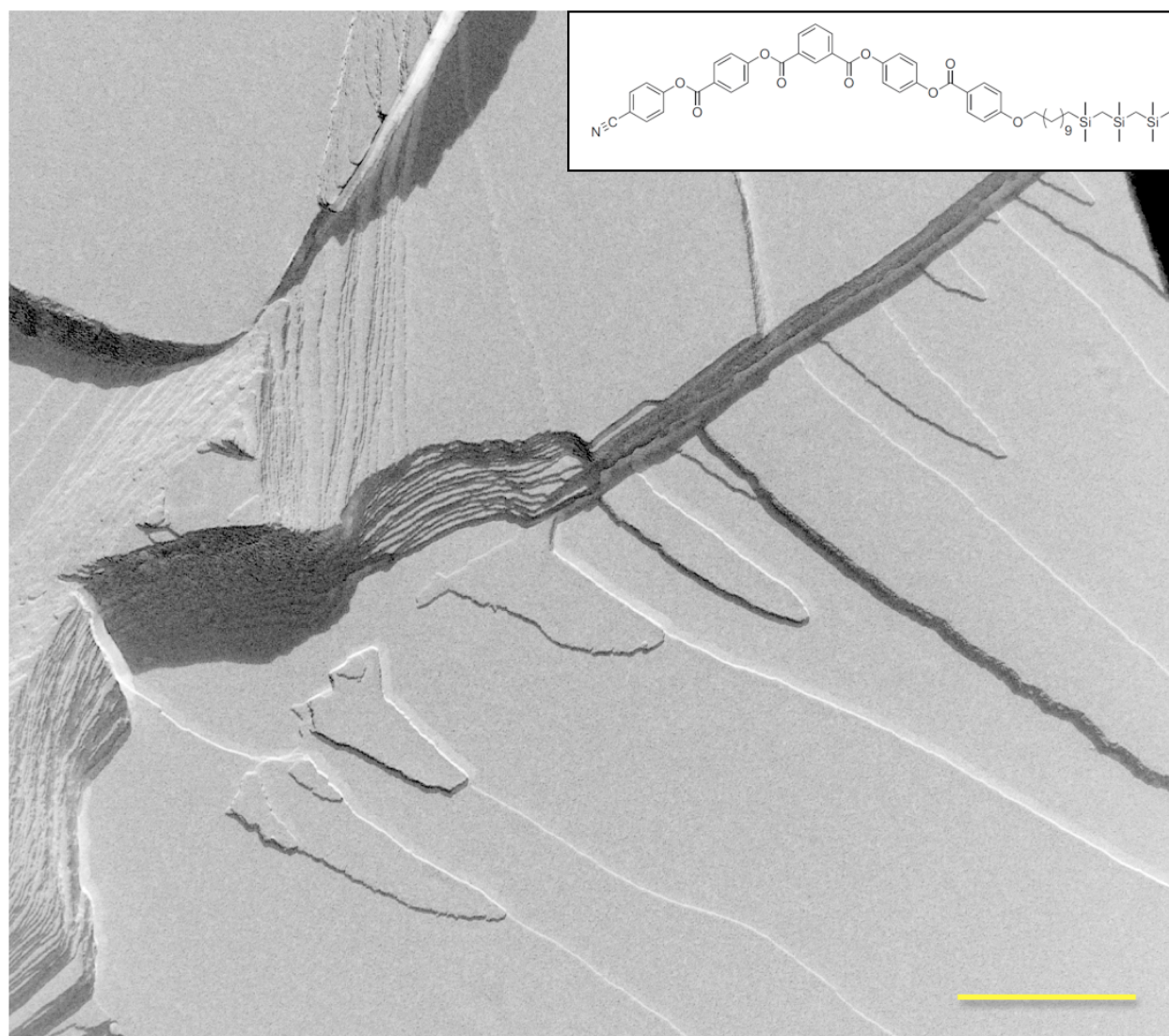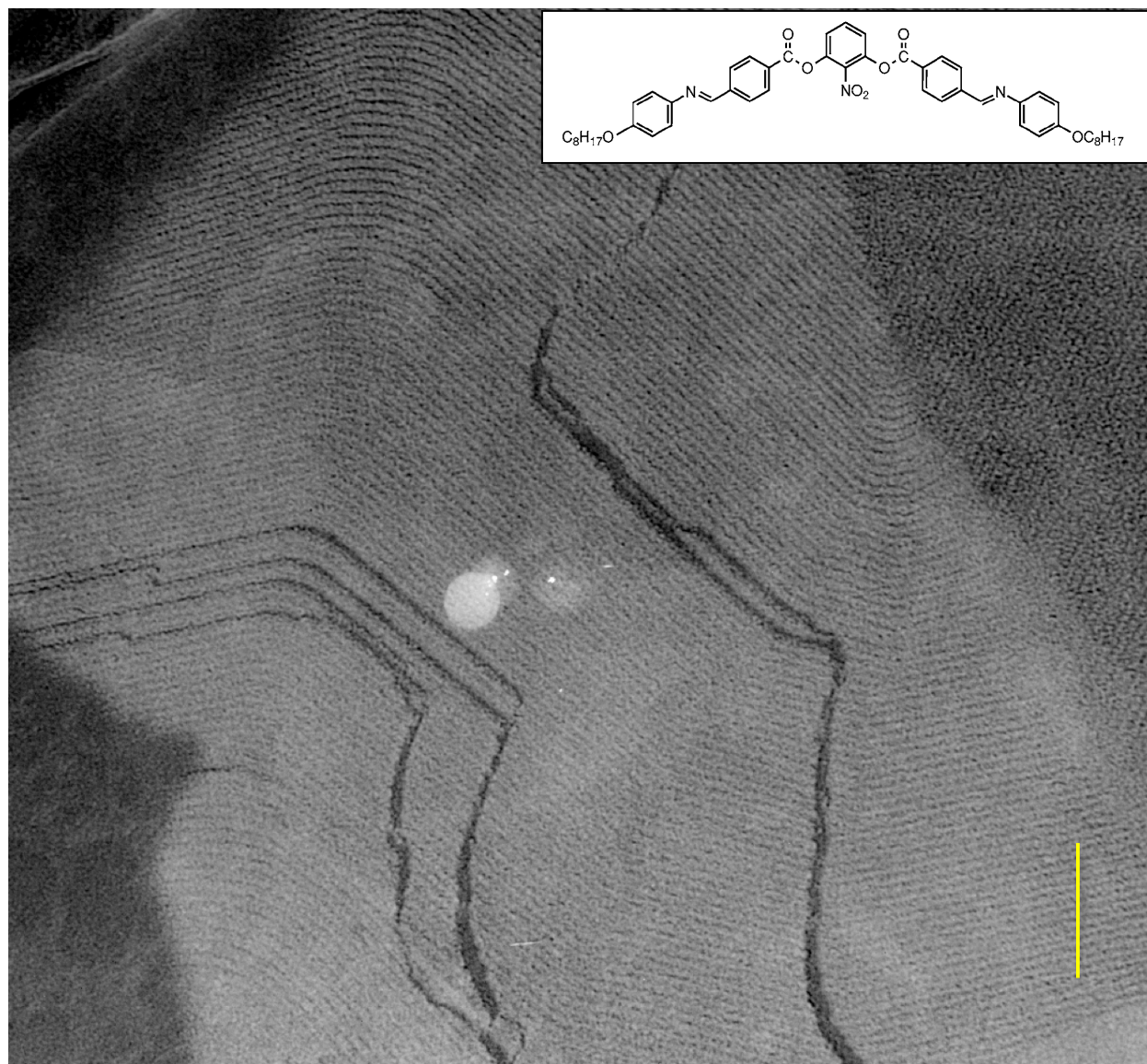
Figure S1

Figure S1 - Fracture area of CB7CB at T = 90ºC where the layer planes are nearly parallel to the image plane over the lower right part of the image ($\psi \sim 0°$) and normal to the fracture plane in the focal conics in the upper left part ($\psi \sim 90°$). Where ψ is small the fracture face becomes rather irregular, in contrast with the case of freeze fracture of smectic layered phases where the layer surfaces are smooth and exhibit distinct layer steps (Figure S2). In the focal conic domains $\psi \sim 90°$ and the fracture periodicity is clear. Scale bars = 100 nm.

Figure S2 - Fracture area of W623 (inset) in its smectic A phase at T = 160 °C. Here the layer planes are nearly parallel to the image plane as for the CB7CB layers in the lower right of Figure S1. However, because of the density modulation and interlayer interfaces characterized by smectic lamellar molecular positioning, the fractures follow the layer interfaces making the fracture surface smooth and terminated only with distinct layer steps, in contrast to the rough surface observed in CB7CB in Figure S1. This difference can be taken as evidence for a layered structure without layer interfaces in CB7CB. Scale bar = 400 nm.

Figure S3 - FFTEM image of 8-OPIMB-NO$_2$ [4] in the B7 phase at T = 150 °C, showing the 1D modulation of smooth layers terminated by layer steps, the typical appearance of a 2D-ordered thermotropic columnar phase in FFTEM. In this case the surfaces of typical fluid smectic bent core layers with spontaneous polar ordering and molecular tilt are largely parallel to the fracture face and modulated by polarization splay stripes. This image may be contrasted with that of CB7CB in Figure S1, which shows a much weaker tendency to form layer steps and smooth faces, which we take as evidence for a TB structure. Scale bar = 100 nm.
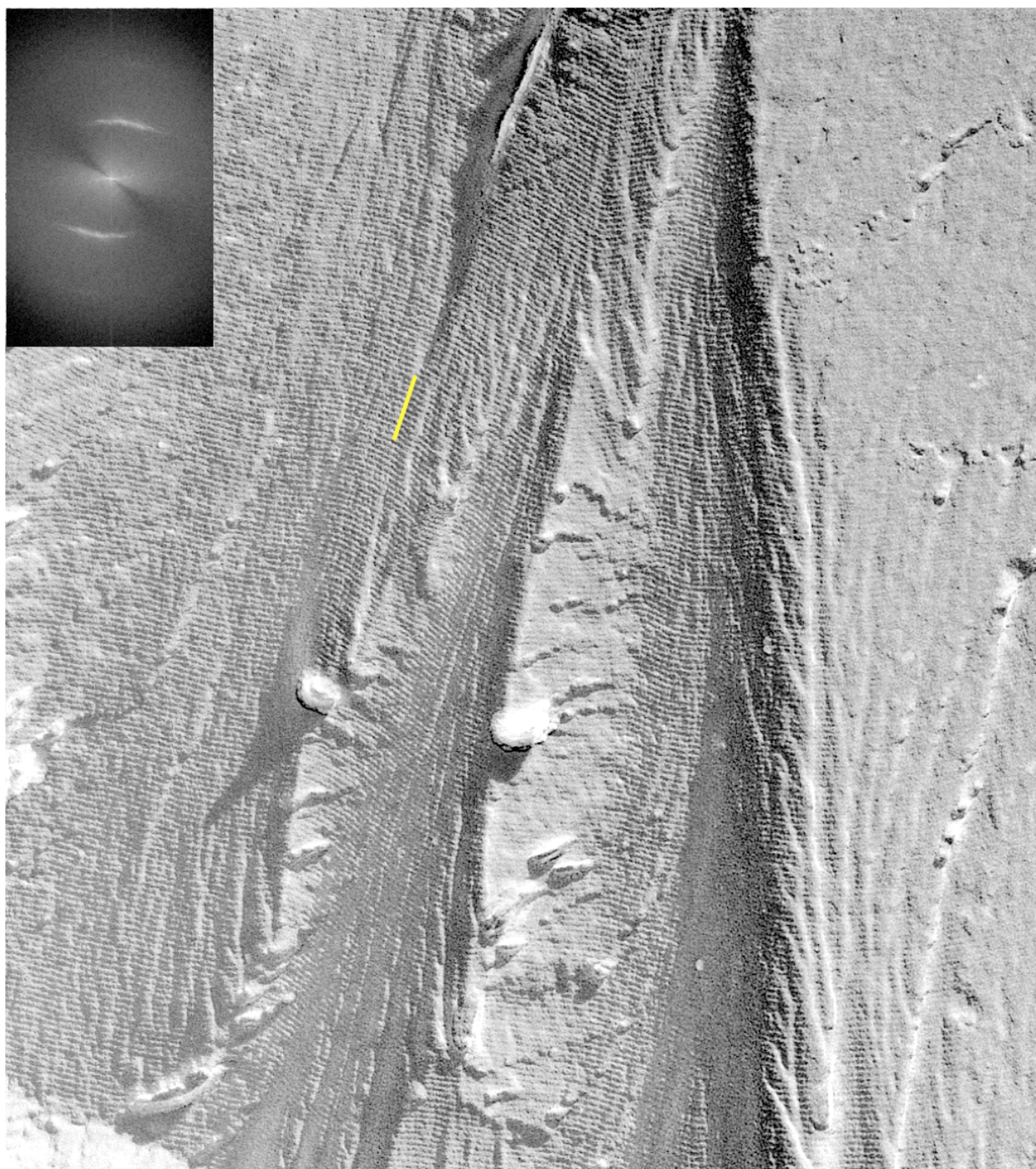
Figure S4 - FFTEM image of CB7CB at T = 90°C. The inset shows the Fourier transform of this optical image calculated using ImageJ. Scale bar = 100 nm.
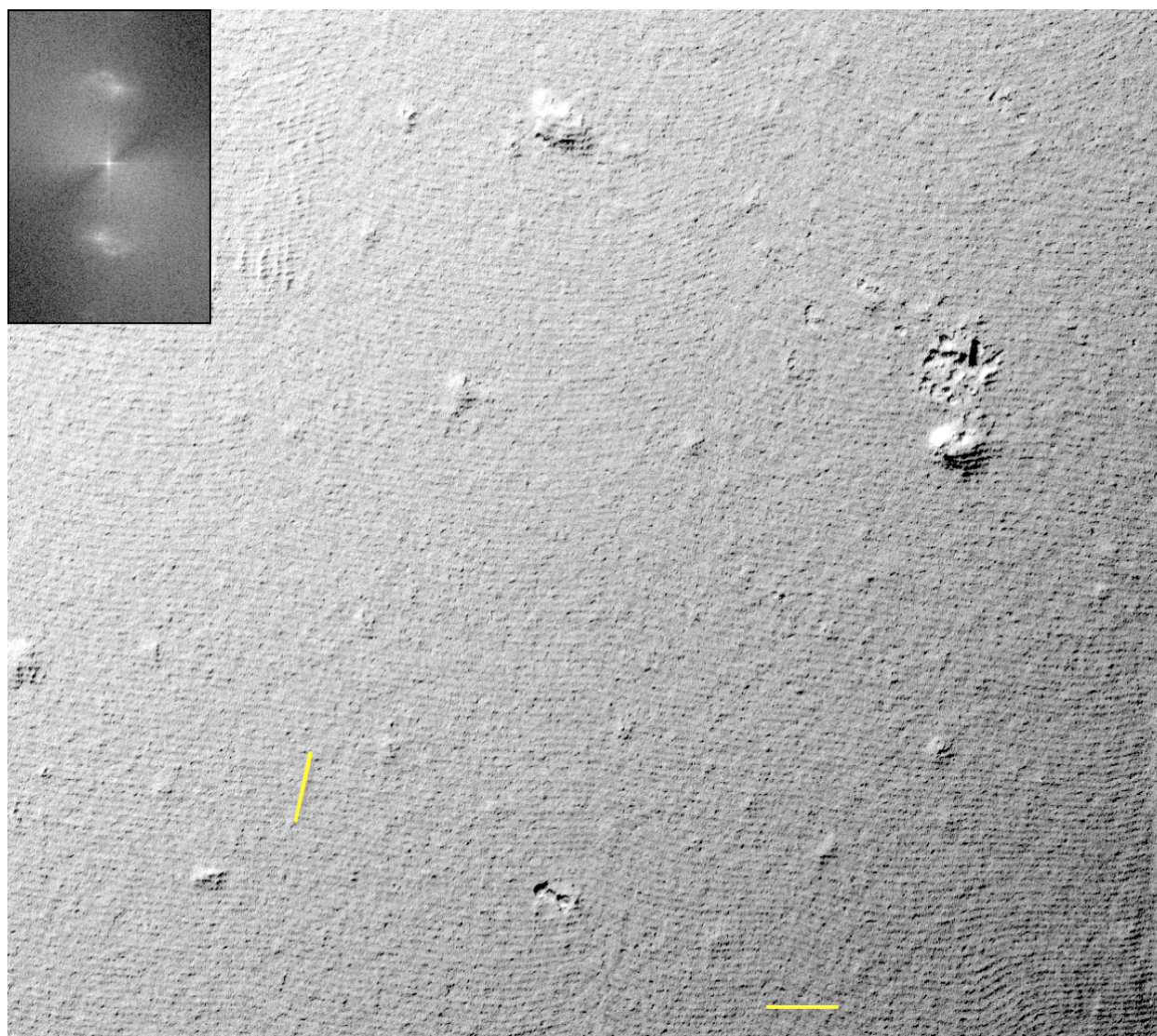
Figure S5 - FFTEM image of CB7CB in the NTB phase at T = 90°C and its Fourier transform (FT) calculated using ImageJ. Here the fuzzy peaks in the FT indicate that the stripe spacing and thus ψ, the angle between the layer normal and the fracture plane normal, varies over the area of the image. $\psi \sim 49°$ at the vertical scale bar. Scale bars = 100 nm.
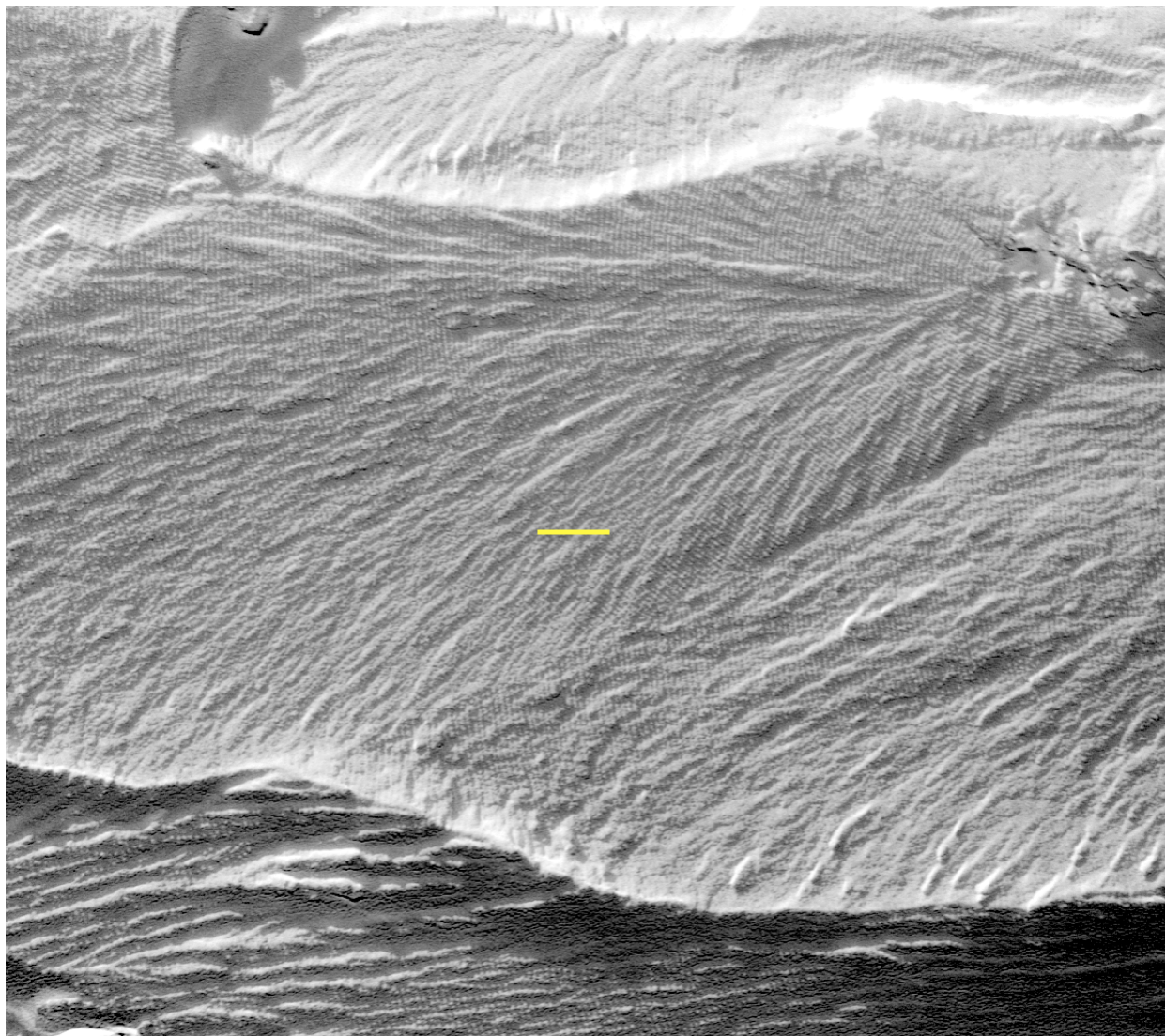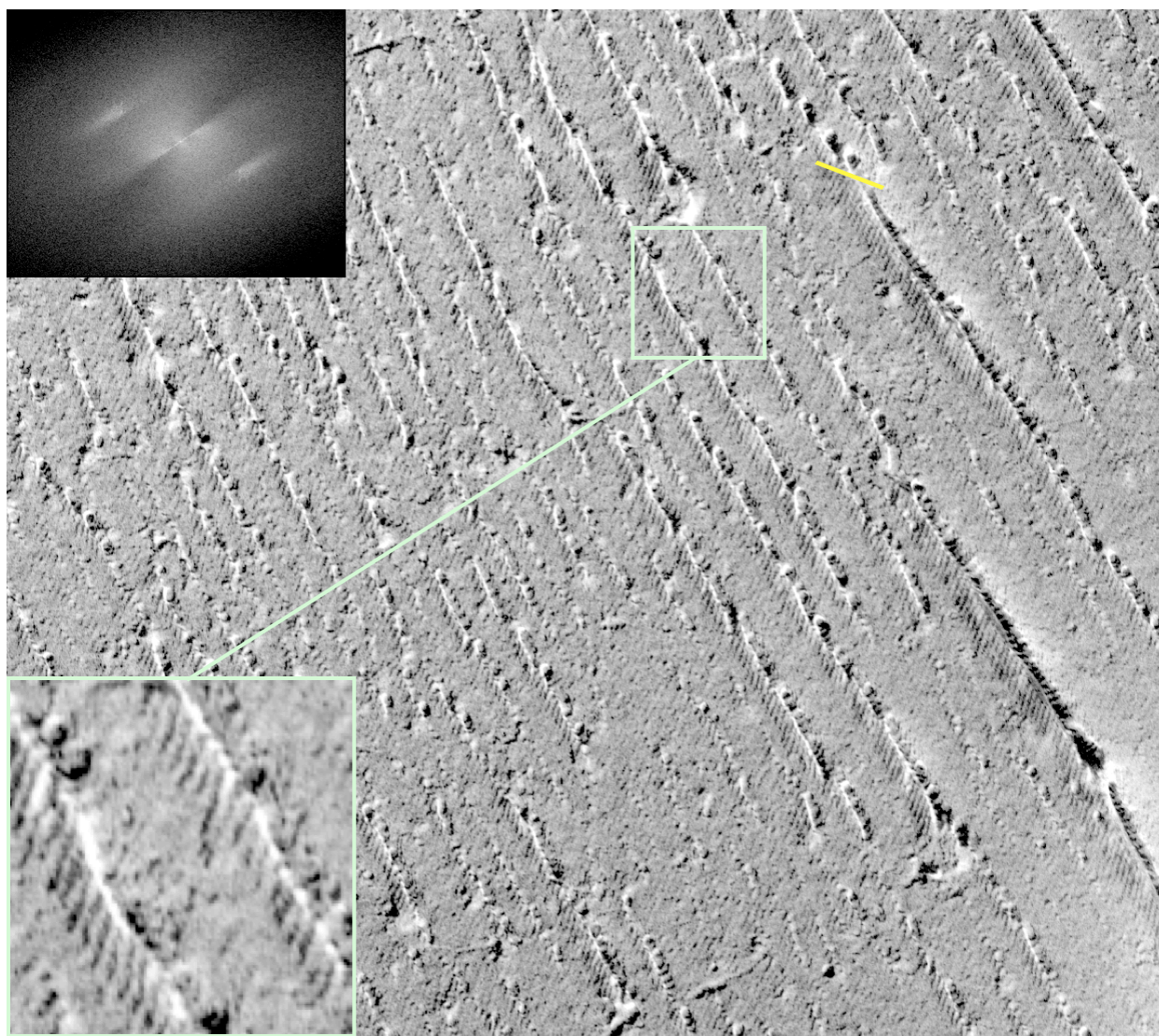
Figure S6 - FFTEM image of CB7CB in the NTB phase at T = 95°C. The general morphology of the modulation patterns and the period, p_{TB}, is similar to that at T = 90°C. Scale bar = 100 nm.

Figure S7 - FFTEM image of CB7CB at T = 95°C exhibiting a chiral structure of the layer modulation and ridges in the fracture texture. This may be a structural manifestation of the inherent chirality of a TB phase, but any definitive interpretation of such an image will require a more detailed modeling of the fracture process. The overall chirality is evident from the lack of reflection symmetry in the Fourier transform of the image (inset). The yellow scale bar is locally parallel to the helix axis. Scale bar = 100 nm.
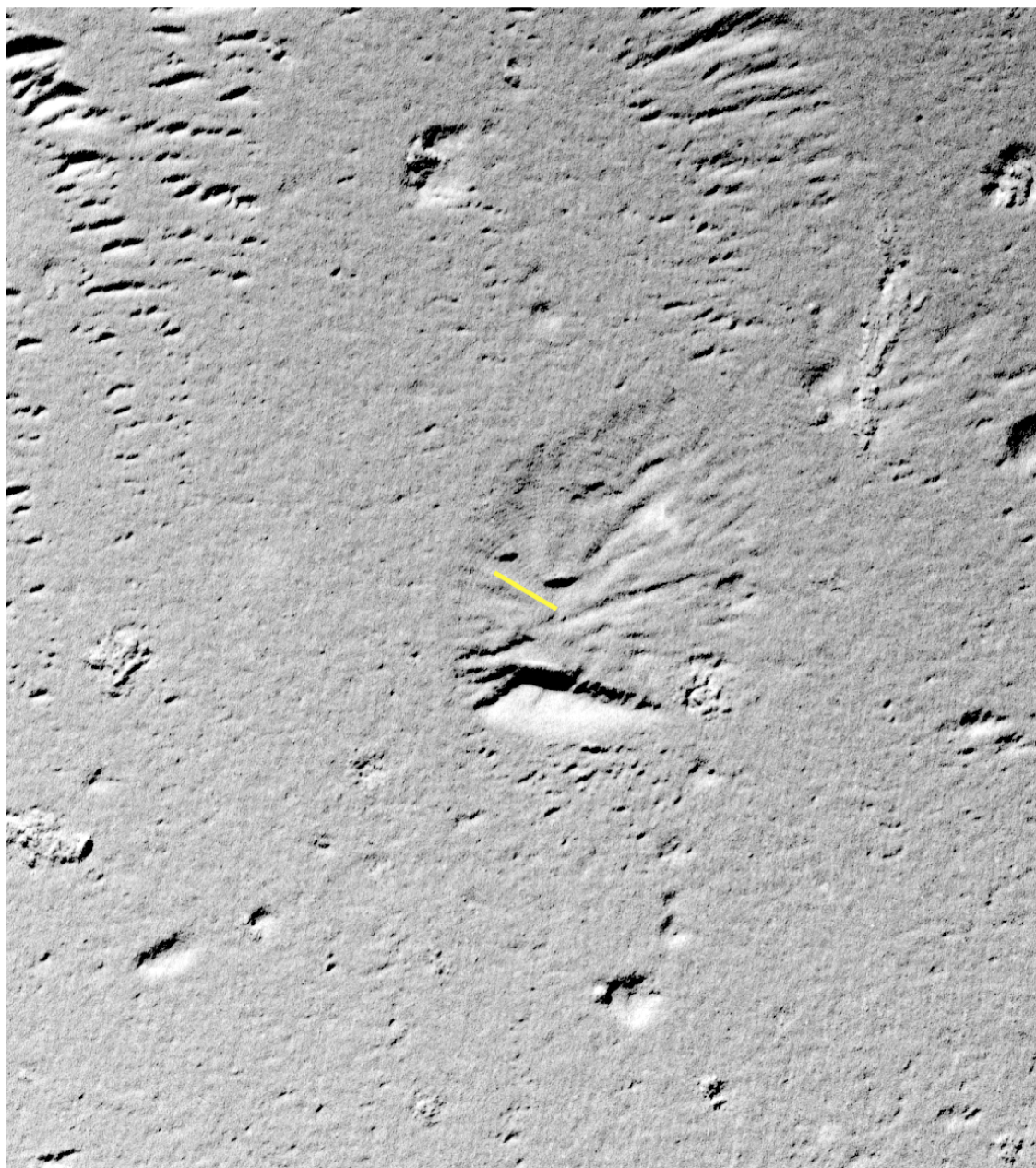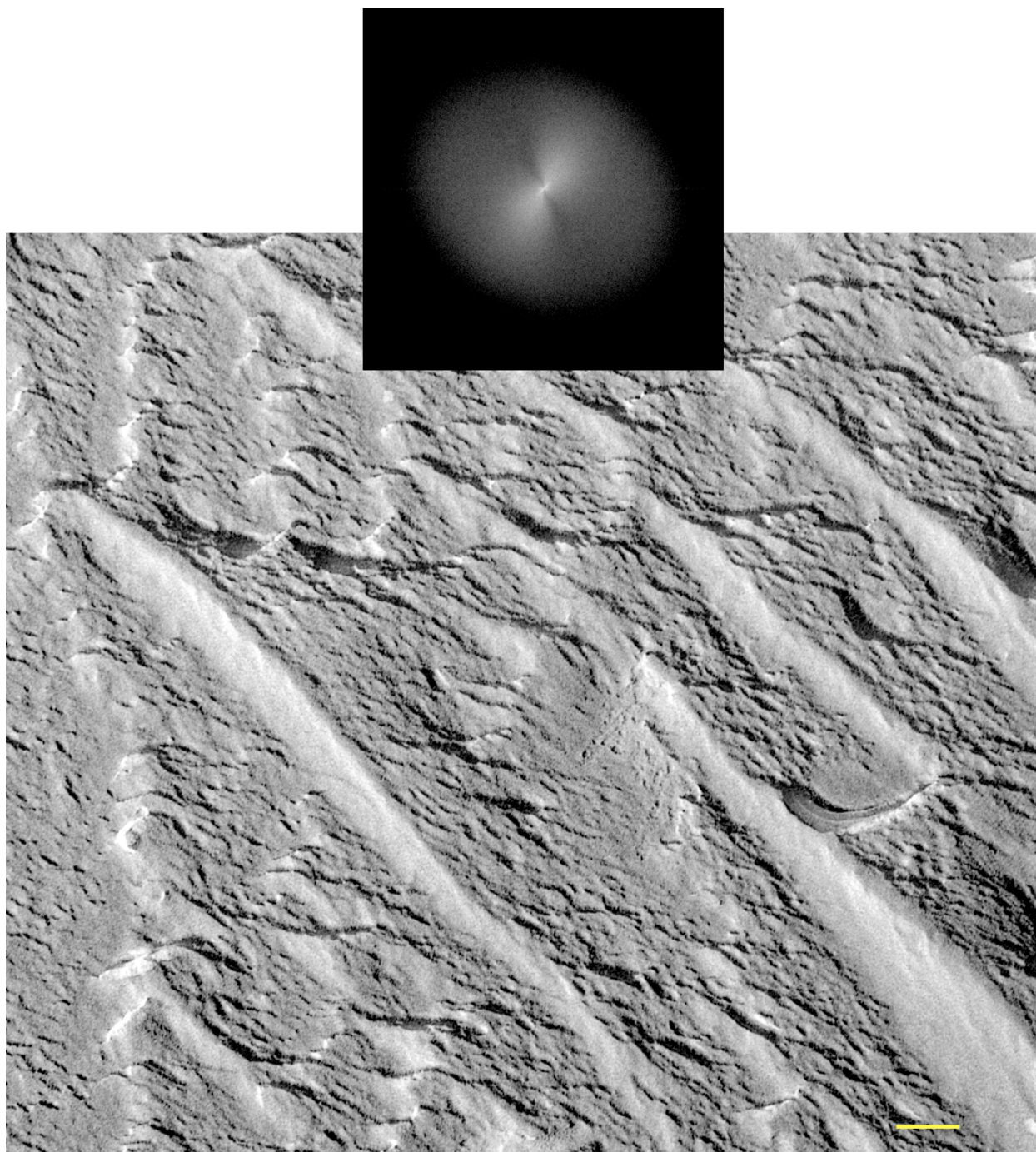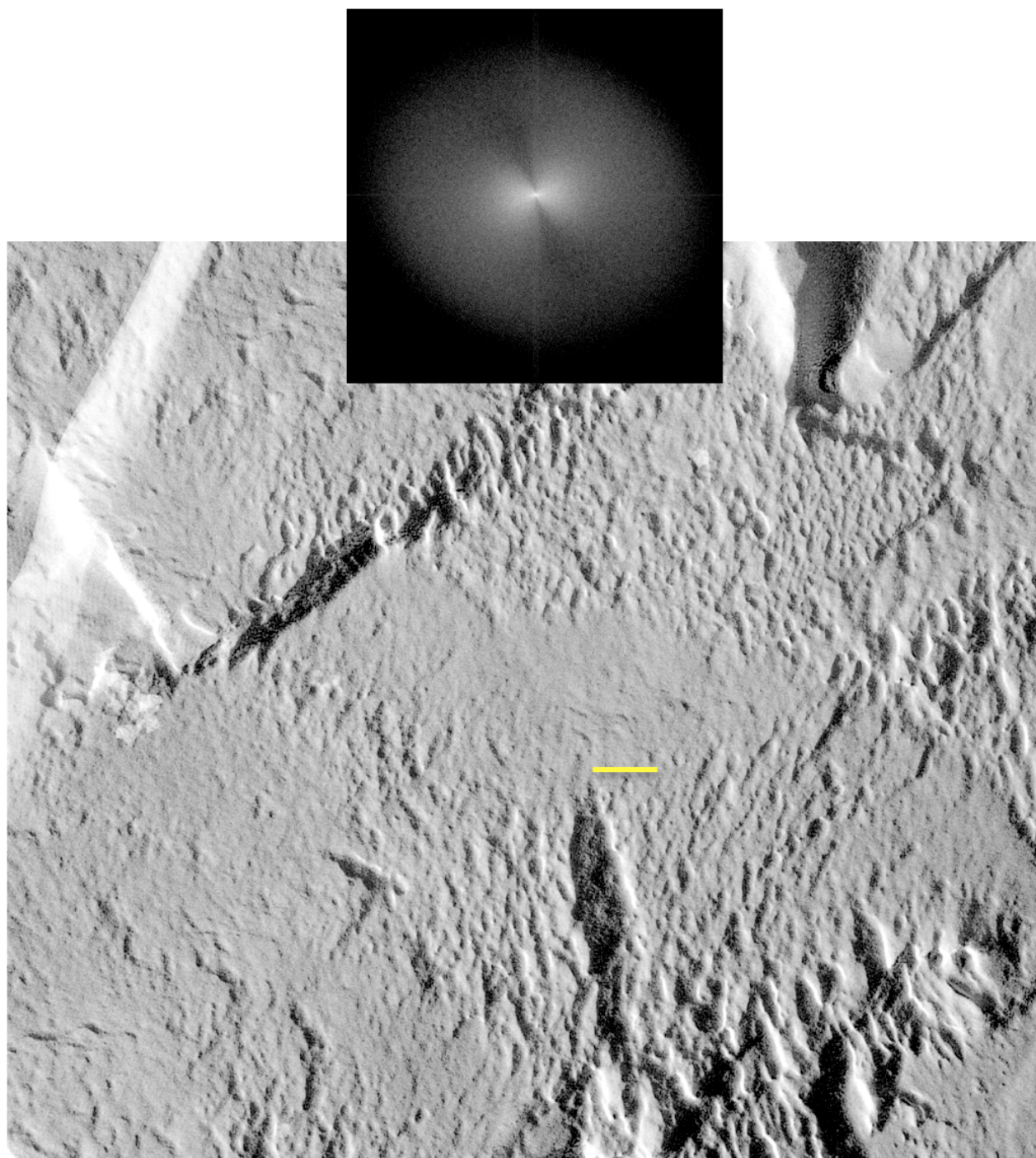
Figure S8 - FFTEM image of CB7CB at T = 100ºC. At this temperature large fracture face areas with stripes coexist with large areas with no stripes, apparently because of coexistence of the NTB with the nematic. This image shows an area with stripes. The general morphology of the modulation patterns and the period, p_{TB}, is similar to that at T = 90ºC. However, the layer modulation pattern on the fracture face is less distinct at this higher temperature near melting of the NTB to the nematic. Scale bar = 100 nm.

Figure S9 - FFTEM image of CB7CB at T = 100ºC. At this temperature large fracture areas with stripes coexist with large areas without stripes, apparently because of coexistence of the NTB with the nematic. This image and its Fourier transform show a domain with no stripes. The Fourier transform (inset) shows no evidence for the TB layering. At T ≥ 105ºC there are no remaining fracture face areas exhibiting stripes. Scale bar = 100 nm.

Figure S10 - FFTEM image of CB7CB at T = 100°C, where large fracture face areas with stripes coexist with large areas without stripes, apparently because of coexistence of the NTB with the nematic. This image and its Fourier transform (inset) show a domain with no stripes. At T ≥ 105°C there are no remaining fracture face areas exhibiting stripes. Scale bar = 100 nm.

Figure S11 - FFTEM image of CB7CB at T = 29°C, in the supercooled NTB phase. The general morphology of the modulation patterns is similar to that at T = 90°C. The period, p_{TB}, is slightly larger. The layer modulation pattern on the fracture face becomes more distinct with decreasing temperature and the fracture surfaces where the layers are normal to the fracture plane become smoother than at T = 90 °C. This suggests that the general preference for fracture normal to the layers in CB7CB is stronger in the NTB glass. Scale bar = 100 nm.
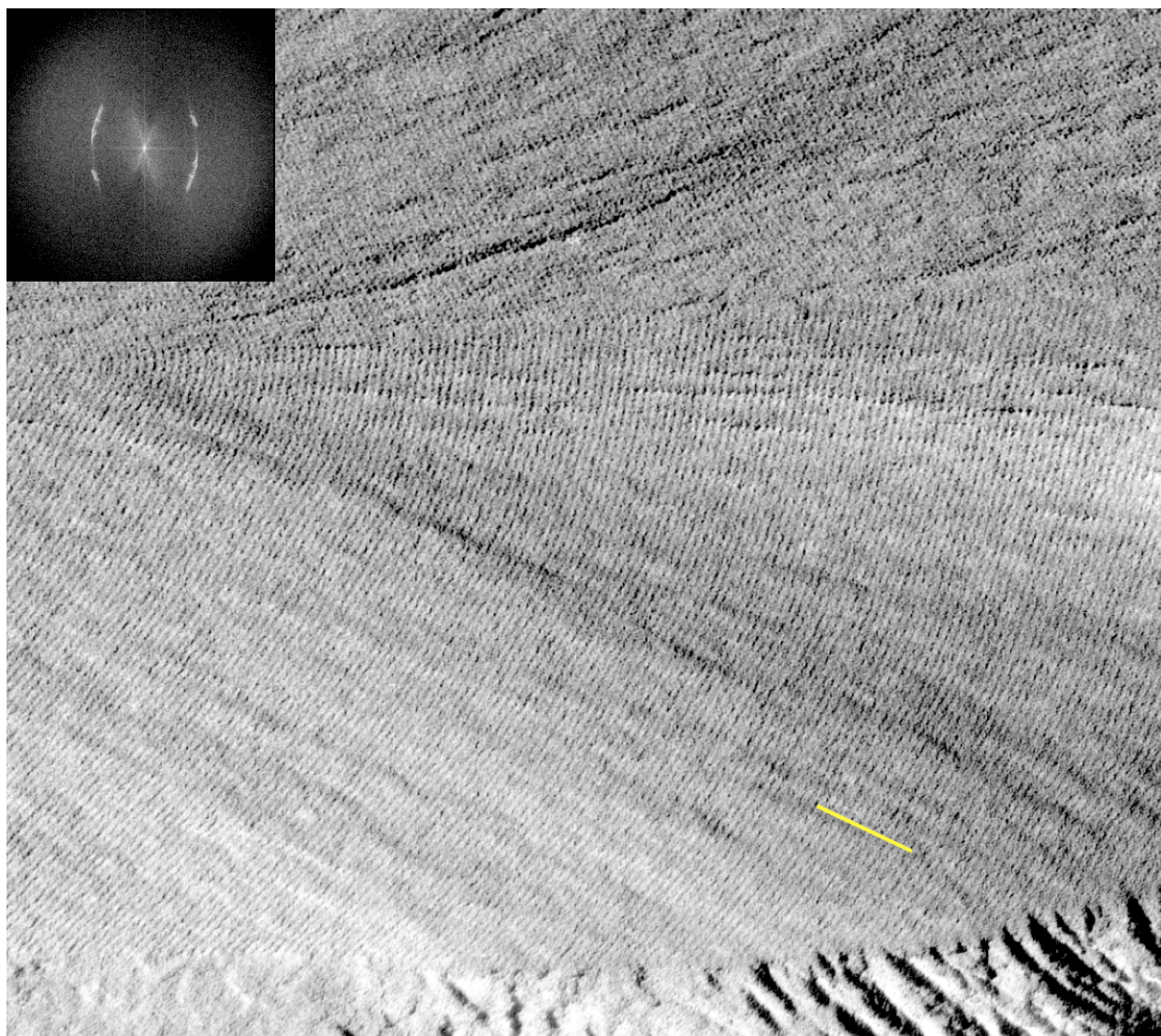
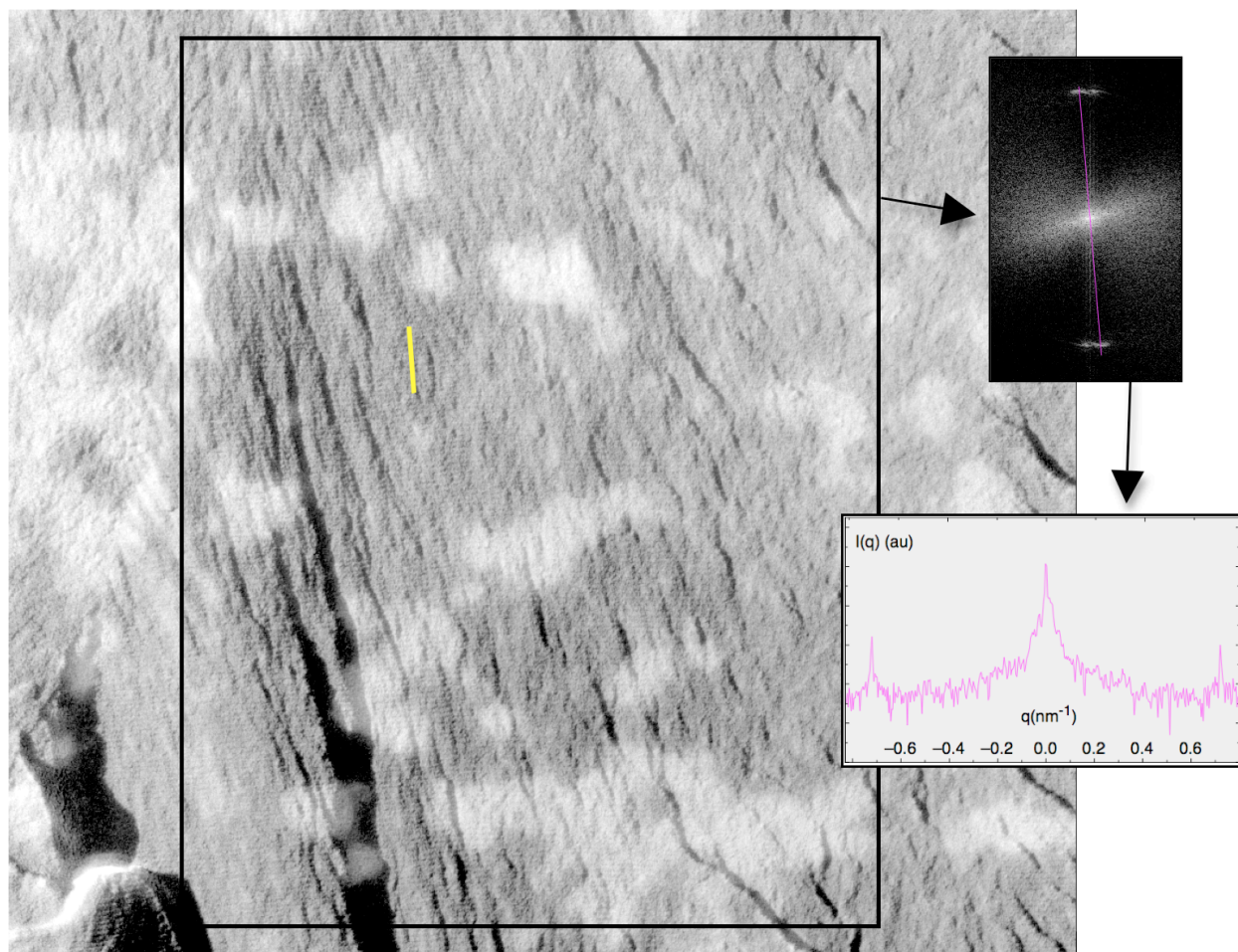*Figure S12* - FFTEM image of CB7CB at T = 29°C, in the supercooled NTB phase. Inset shows the image Fourier transform. Scale bar = 100 nm.

*Figure S13* - FFTEM image of CB7CB at T = 29°C, in the supercooled NTB phase, showing the Fourier transform of the intensity distribution of the image in the selected (black box) area, and the profile of the Fourier transform along the magenta line, showing the first order Bragg reflection peaks from the layer modulation. The modulation peaks are sharp, of HWHH ~ 1 pixel in q-space, indicating that the coherence length for loss of layer periodicity in the direction normal to the layers is longer than the Fourier transform resolution. Since generally the layer spacing, d_p, in the periodic patterns in the FFTEM images will variable due to variations in ψ, the images where d_p is most uniform, such as the selected area in this one, best reflect the spatial variation of the bulk spacing d. Scale bar = 100 nm.
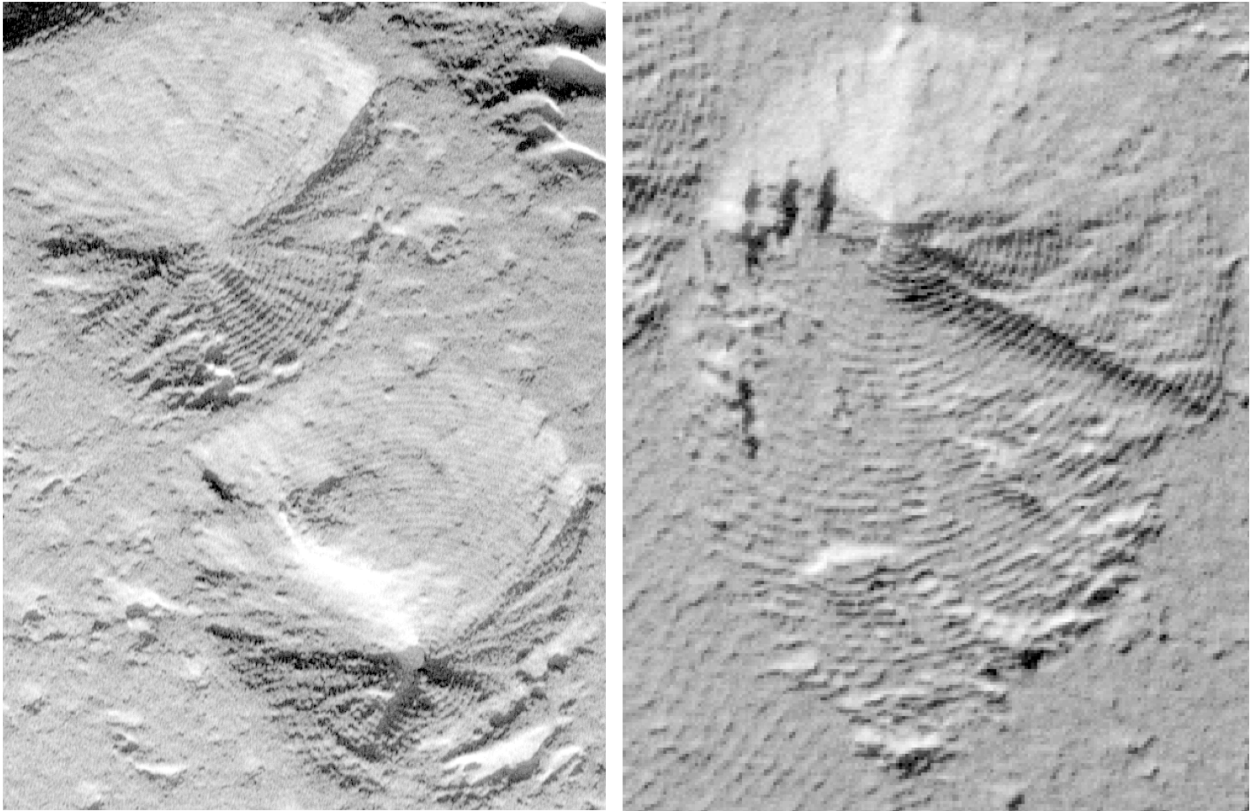
Figure S14 - FFTEM image of CB7CB NTB phase, showing commonly observed circular focal conic domains that produce a cone shaped hill where they terminate in the fracture plane (left). Some of these have a distinctly teardrop shape (right).
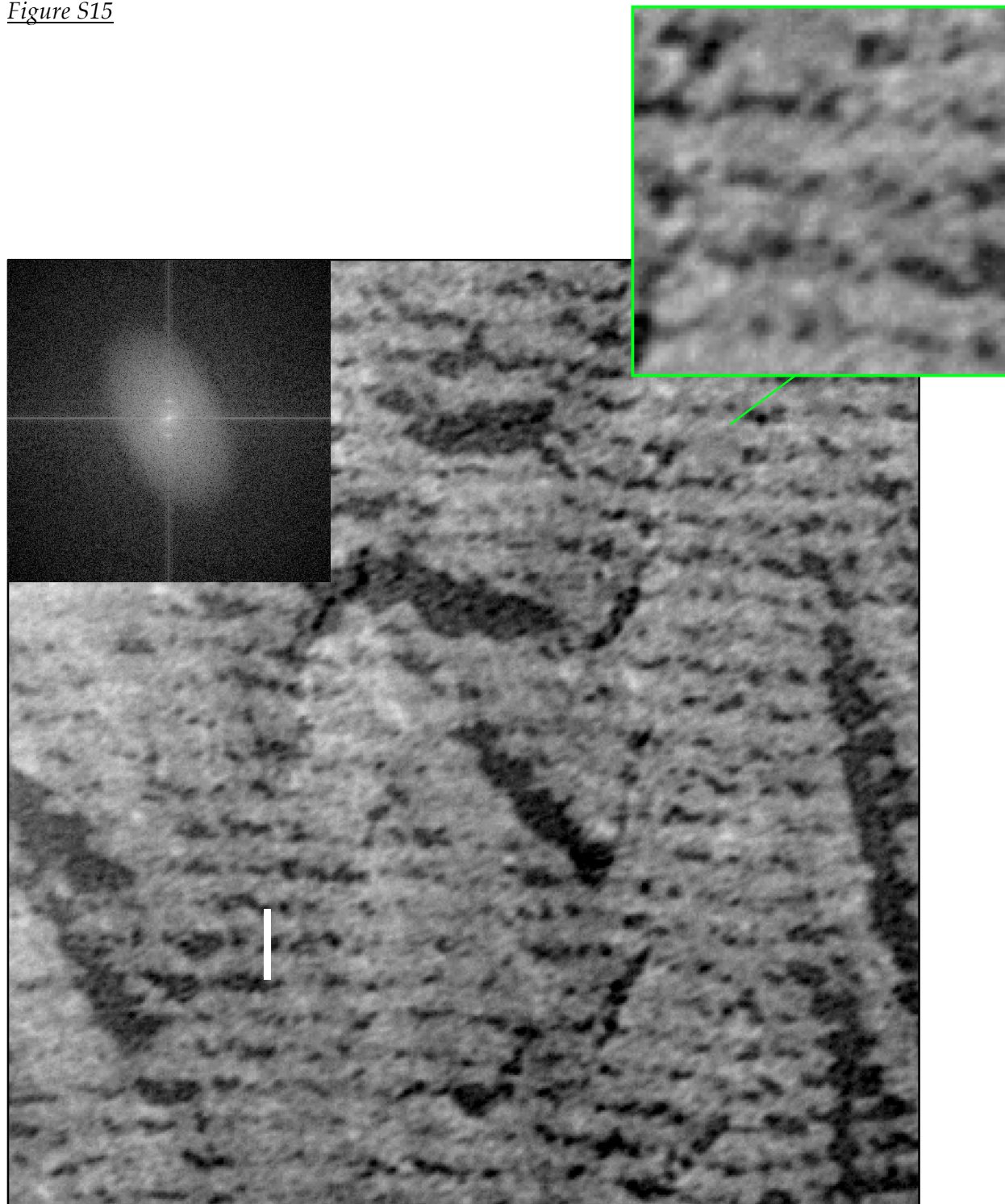
Figure S15 - Higher magnification image of CB7CB quenched at T = 95 °C. The inset shows the oblique striations giving the oblique diffuse oval hump around q = 0 in the FFT. These structures may reflect the local chirality of the TB helix, but confirmation of this will require higher resolution techniques. The inset also serves to indicate the inherent resolution of the freeze fracture technique, here on the order of 0.5nm. Scale bar = 16 nm.
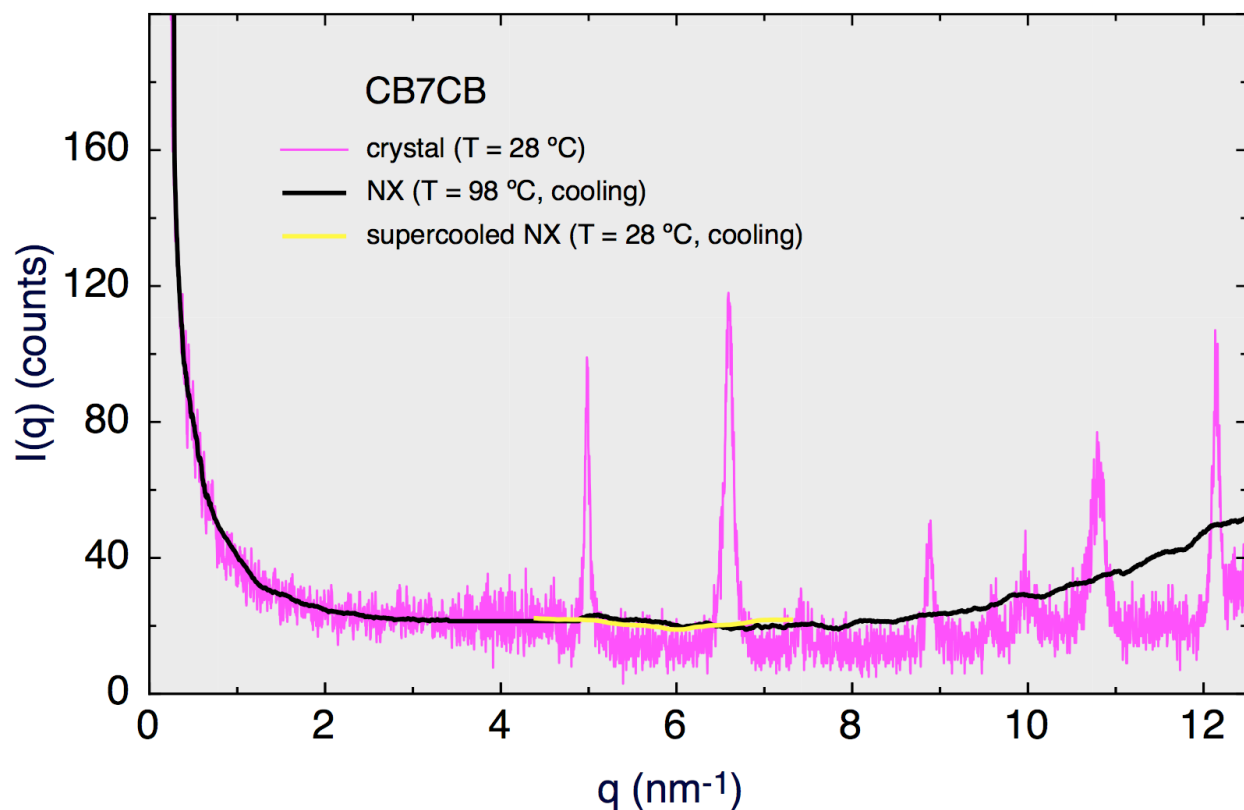
Figure S16 – Powder XRD scans of the crystal phase of CB7CB at room temperature (magenta), the NTB phase, obtained upon cooling from the isotropic and nematic (black), and the supercooled NTB phase (yellow). The scan in the supercooled NTB phase, over the limited range, $0.45nm^{-1} < q < 0.7nm^{-1}$, probes the intensity of the two large crystal peaks. Upon cooling from the NTB to room temperature at an intermediate rate, i.e., over a 1 to 60 second interval, the thermotropic NTB phase supercoools into an NTB glass, as evidenced by the complete absence of the crystal peaks. These may reappear after several days, or as diffuse reflections for very slow cooling.
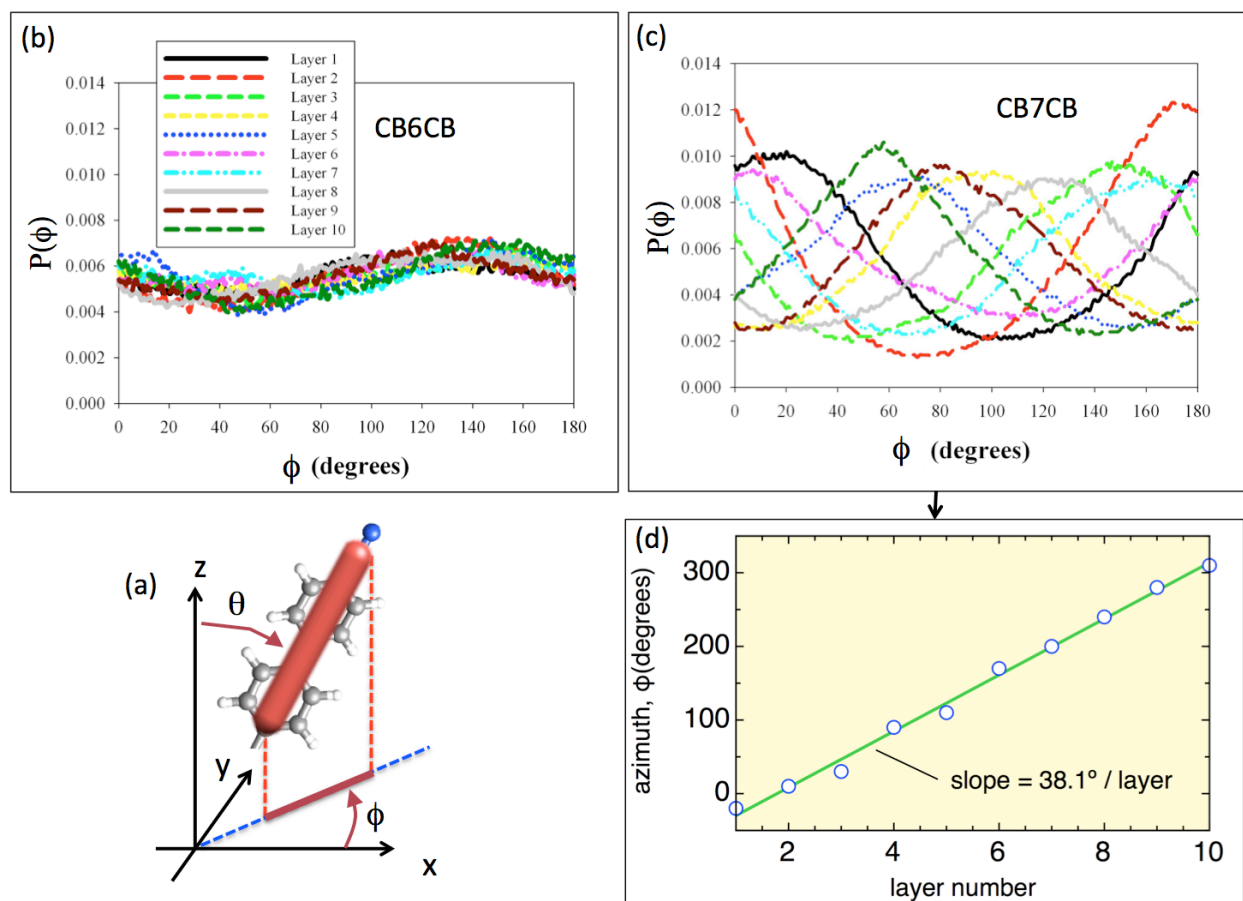
Figure S17 – Comparison of the distributions of ϕ, the azimuthal orientation of the CB unit vector projection into x-y plane (a) obtained in the MD simulations, as function of a series of z values spaced by $L_z/10$. (b) For CB6CB the distribution is nearly uniform for all layers, i.e. indicating that x-y projections are oriented randomly in the layers. (c) For CB7CB, however, each layer has a preferred azimuthal orientation angle that advances in helical fashion with advancing vertical position. (d) Fitting the distribution maxima gives an advance of $38.1°$/layer, or a helical pitch in this case of $360/38.1 = 0.945\ L_z$.

In CB6CB the nematic eigenstate is along z, with a half molecular core nematic order parameter of 0.82. In CB7CB the nematic eigenstate is the perfect heliconical director precession, and the order parameter for fluctuations of the half molecular cores away from this eigenstate is is 0.73. The eigenstate cone angle is $\theta_{TB} = 25°$ and the pitch $p_{TB} = 8.3$nm.
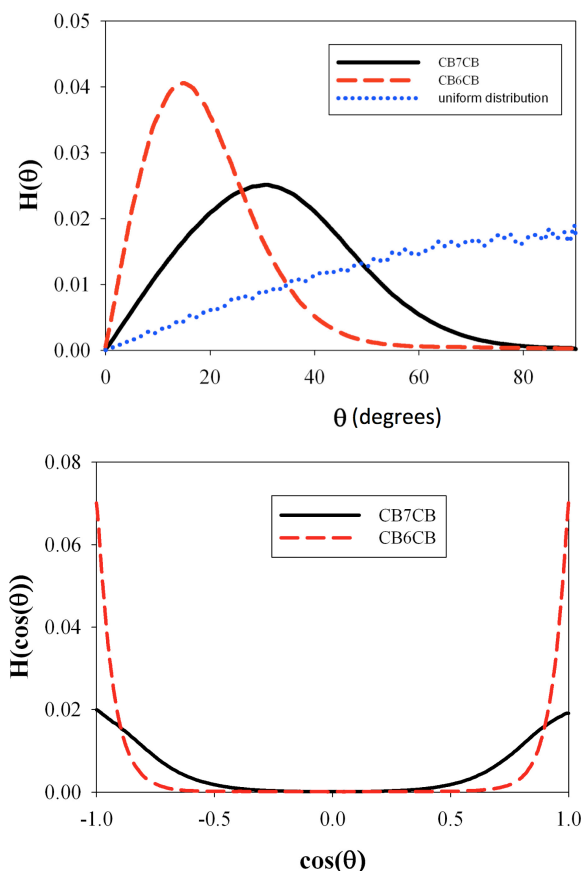
Figure S18 – H(θ), the distribution of the tilt orientations of the CB unit vector with respect to z (defined as θ in Figure S17) obtained from the MD simulations. H(θ) is more strongly peaked near θ = 0º for the uniformly nematic CB6CB, but pushed to larger angle in the conical helix structure of CB7CB.

SUPPORTING INFORMATION REFERENCES

1 Borodin O (2009) Polarizable force field development and molecular dynamics simulations *of* ionic liquids *J. Phys. Chem.* B **113**: 11463-11478.

2 Martyna GJ, Tuchkerman M, Tobias DJ, Klein MJ (1996) Explicit reversible integrators for extended systems dynamics *Mol. Phys.* **87**: 1117-1157.

3 Palmer BJ (1993) Direct application of SHAKE to the velocity-c verlet algorithm *J. Comput. Phys.* **104**: 470-472.

4 Pelzl G, Diele S, Weissflog W (1999) Banana-shaped compounds—a new field of liquid crystals *Adv. Mat.* **11**: 707-724.